



Article

Validation and Evaluation of a Behavioral Circuit Model of an Enhanced Electrostatic MEMS Converter

Mona S. Salem¹, Abdelhalim Zekry¹ , Mohamed Abouelatta¹, Ahmed Shaker^{2,*}  and Marwa S. Salem^{3,4}

- ¹ Electronics and Communications Engineering Department, Faculty of Engineering, Ain Shams University (ASU), Cairo 11517, Egypt; monabasyoni@gmail.com (M.S.S.); aaazekry@hotmail.com (A.Z.); m.abouelatta@eng.asu.edu.eg (M.A.)
- ² Physics and Mathematics Engineering Department, Faculty of Engineering, Ain Shams University (ASU), Cairo 11517, Egypt
- ³ Department of Computer Engineering, Computer Science and Engineering College, University of Ha'il, Ha'il 55211, Saudi Arabia; marwa_asu@yahoo.com
- ⁴ Department of Electrical Communication and Electronics Systems Engineering, Faculty of Engineering, Modern Science and Arts (MSA) University, Cairo 12566, Egypt
- * Correspondence: ahmed.shaker@eng.asu.edu.eg

Abstract: In this current study, the validation and evaluation of a behavioral circuit model of electrostatic MEMS converters are presented. The main objective of such a model is to accurately find the converter behavior through the proper choice of its circuit elements. In this regard, the model enables the implementation of the electrostatic MEMS converter using commercially available off-shelf circuit elements. Thus, the overall vibration energy harvesting system can be implemented and tested without the need for fabricating the converter. As a result, the converter performance can be verified and evaluated before its fabrication which saves the expenses of fabricating trailed prototypes. To test the model, we apply it to an enhanced converter in which the conventional electrostatic MEMS converter is modified by depositing the tantalum pentoxide, Ta₂O₅, a high dielectric constant material, on its fingers' sidewalls. Such a deposition technique causes an appreciable increase in the overall converter capacitance and, in turn, the output power, which is boosted from the range of μW to the range of mW. Next, the converter behavioral circuit model, which is based on representing its capacitance variations with respect to the input displacement, x caused by the vibration signal, $C-x$ curve, is built up. The model is qualitatively validated and quantitatively evaluated. The enhanced converter performance is investigated through the interaction of its model with the power conditioning circuit. From the simulation results, it is revealed that the converter behavioral circuit model accurately accomplishes the vibration energy conversion operation. As a result, the specification of the required controlling pulses for the converter operation is accurately determined. Finally, the model accuracy is validated by calibrating its performance with a traditionally simulated and fabricated electrostatic MEMS converter.

Keywords: behavioral; circuit model; MEMS converter; vibration; energy harvesting; $C-x$ curve



Citation: Salem, M.S.; Zekry, A.; Abouelatta, M.; Shaker, A.; Salem, M.S. Validation and Evaluation of a Behavioral Circuit Model of an Enhanced Electrostatic MEMS Converter. *Micromachines* **2022**, *13*, 868. <https://doi.org/10.3390/mi13060868>

Academic Editor: Faisal Mohd-Yasin

Received: 24 April 2022

Accepted: 23 May 2022

Published: 31 May 2022

Publisher's Note: MDPI stays neutral with regard to jurisdictional claims in published maps and institutional affiliations.



Copyright: © 2022 by the authors. Licensee MDPI, Basel, Switzerland. This article is an open access article distributed under the terms and conditions of the Creative Commons Attribution (CC BY) license (<https://creativecommons.org/licenses/by/4.0/>).

1. Introduction

During the previous two decades, a significant enhancement in the development of low-power, portable, small size, and remote devices has been achieved. This enhancement causes the replacement of the traditional with nontraditional power sources. Recent research concentrates on harvesting energy from the environment. The reason is that, in some applications which are in an inaccessible environment or which have high maintenance costs, energy harvesting becomes essential. Wireless sensor nodes in remote areas, biomedical devices, and implanted health trackers are examples of applications that require energy harvesting systems [1–4]. Energy harvesting is the direct conversion of environmental energy such as thermal, wind, vibration, and solar energy into electrical energy [5–8]. A

MEMS vibration energy harvester is mainly a spring-mass system. It has one or more resonance frequencies of vibration. Based on the mechanism of transfer, most MEMS vibration energy harvesters are classified into three different types: piezoelectric [9,10], electromagnetic [11,12], and electrostatic harvesters [13]. In an electromagnetic energy harvester, the losses caused by its coil resistance are one of its major drawbacks. In addition, it requires complex fabrication processes which have low process compatibility [14]. Electrostatic harvesters, on the other hand, can be easily fabricated using standard micro-machining processes [15–18].

It is important to determine which MEMS transducer type satisfies the best power density in a certain energy harvesting system. It is shown that, at low accelerations, electrostatic harvesters are better than piezoelectric harvesters because of the lower energy losses and vice versa at high accelerations. At very high accelerations, the performance of piezoelectric energy harvesters is severely degraded because of the dielectric breakdown limit. Thus, the electrostatic harvesters are better at very high accelerations. Based on such a comparison, it is clear that the optimal transduction mechanism depends on the harvesting acceleration, operating frequency, and device size [19–25]. Moreover, electrostatic harvesters are based on the capacitive sensing mechanism, which is the main dominant method for micromachined applications. The reason is that it is compatible with all the fabrication approaches and stiffness [26–29]. Recent research studies focus on enhancing the electrostatic MEMS converter performance by mainly increasing its output power. Unfortunately, the converter output power is still in the range of μW to fractions of mW [30–33]. Moreover, there is another direction in recent research that focuses on the accompanying circuit, which is necessary for delivering the output power of the converter to the load, the power conditioning, and the power controlling circuits. Also, such a direction still needs more research efforts [34–37].

Our research group conducted previous efforts in this field. We had already developed a proposed model for the electrostatic MEMS converter, which satisfied the charge transfer between the converter model and the system storage element. However, it did not achieve a good agreement between the calculated converter output power and the simulated output power gained from the vibration energy conversion operation [38–40]. Furthermore, the transitions between the system elements need to be restudied and re-simulated as they were not exactly representing the specific operation during each transition. In addition, in our previous work, the output power that was achieved from the designed converter was relatively low, 0.122 mW [38–40].

The main contribution of this research work is to reinvestigate our promising proposed converter behavioral circuit model. Thus, by using the enhanced proposed model, the difficulties of practically testing the designed converter due to the unavailability of the fabrication facilities could be overcome. Furthermore, the electrostatic MEMS converter requires deep reactive ion etching (DRIE) for large aspect ratios [41,42], which is considered a difficult fabrication process to be available in most cleanrooms. Thus, in this work, firstly, the performance of the conventional electrostatic MEMS converter is improved by depositing the high dielectric material, Ta_2O_5 , on its sidewall fingers. As a result, the converter output power is boosted to the range of a few mW which is considered a remarkable enhancement when compared with the most recent research work [30–33]. Secondly, the main contribution of this work is to illustrate the converter behavior based on its $C-x$ curve, which demonstrates the converter capacitance changes with respect to the displacement, x , caused by the input vibration signal. Thus, the performance of our previously proposed behavioral circuit model for the MEMS converter can be enhanced. Such enhancement aims to achieve a good agreement between the calculated converter output power and the simulated output power gained from the vibration energy conversion operation. As a result, our proposed model will be adaptive to be applied to any other MEMS converter. Thus, by using this model, the implementation and testing of the MEMS converter along with the overall vibration energy harvesting system using commercially available off-shelf components can be easily achieved. As a result, the

designed converter performance can be cheaply tested and evaluated before going through the costly fabrication procedures. Before implementing the model, it must be qualitatively validated and quantitatively evaluated to confirm its vitality in well demonstrating the converter performance.

Moreover, the interaction between the model and the power conditioning circuit enables the accurate specification of the required controlling pulse for the converter operation. As a result, the converter conditioning and controlling circuits, along with the whole vibration energy harvesting system, can be easily designed, implemented, and tested without the need for sophisticated analytical modeling [34–37].

The paper is organized as follows. In Section 2, the electrostatic MEMS converter, along with its main technological parameters, are presented. In Section 3, the main governing analytical equations for the converter performance are illustrated. Moreover, the maximum voltage, V_{max} , which is one of the main system constraints, is simulated and determined. After that, in Section 4, the electrostatic MEMS converter behavior based on its $C-x$ curve is qualitatively explained. Then, in Section 5, the proposed behavioral circuit model of the converter is given. Section 5 illustrates the qualitative validation and the quantitative evaluation of the converter model. Finally, a summary of the important findings and conclusions of this work is offered in Section 6.

2. Electrostatic MEMS Converter and Main Parameters

The in-plane gap-closing electrostatic MEMS converter is considered the most commonly used type of electrostatic MEMS converter as it gives the highest power density [25]. Figure 1a demonstrates the conventional in-plane gap-closing electrostatic MEMS converter, while Figure 1b shows the details of its main technological parameters, respectively [42]. The converter comb drive technological parameters are identified in Table 1. Such parameters will be used in building up the converter behavioral model in the coming sections. The converter comb drive has two main capacitances according to its fingers position with respect to its fixed comb and anchors, which are minimum capacitance (C_{min}) and maximum capacitance (C_{max}), expressed by Equations (1) and (2), respectively.

$$C_{min} = \frac{4N_g \epsilon_0 \epsilon_r L_f t}{d_{nom.}} \quad (1)$$

$$C_{max} = \frac{4N_g \epsilon_0 \epsilon_r L_f t d_{nom.}}{(d_{nom.}^2 - Z_{max}^2)} \quad (2)$$

where: N_g is the number of fixed/movable fingers; $d_{nom.}$ is the nominal gap between fingers at rest position, and Z_{max} is the maximum deflection of the converter springs from their rest position [42]. In this work, the technological parameters of the converter shown in Figure 1b are selected as a case study to investigate its performance [19,43].

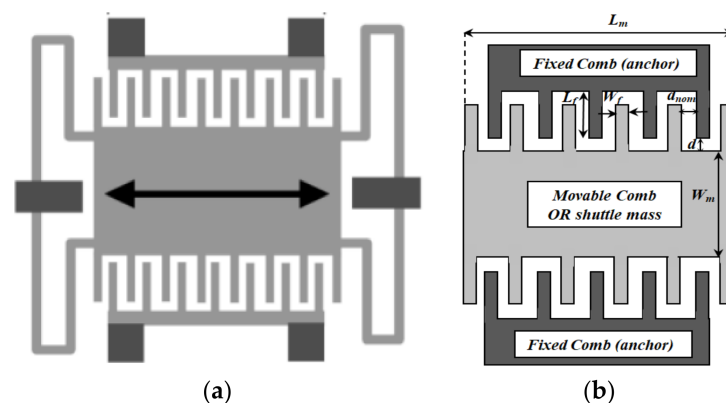


Figure 1. (a) The conventional gap-closing electrostatic MEMS converter and (b) A detailed description of the converter comb drive parameters [42].

Table 1. Main technological parameters of the conventional gap-closing electrostatic MEMS converter comb drive for the case study.

Symbol	Technological Parameter	Value
L_f	Finger Length	512 μm
W_f	Finger Width	7 μm
$d_{nom.}$	Nominal Gap between Fingers at rest position	7 μm
d	Dielectric Distance	50 μm
L_m	Shuttle Mass Length	1 cm
W_m	Shuttle Mass Width	0.3 cm
$L_{terminal}$	Positive Terminal Length	100 μm
$W_{terminal}$	Positive Terminal Width	100 μm
N_g	Number of fixed or movable fingers	476
t	Device thickness	500 μm

Referring to Table 1, the main objective of applying such a case study is to increase the converter capacitance; thus, its output power will increase. Based on the case study [19], to increase the converter capacitance, the nominal gap between its fingers at the rest position ($d_{nom.}$) should be minimized. Its minimum value is limited to 7 μm based on the fabrication constraints [19]. Moreover, the converter thickness (t) should be increased. It is set to be 500 μm as a case study [19] which satisfy the required enhancement of the converter capacitances, taking into consideration that it requires a lower fabrication cost. Moreover, the finger length (L_f) should be maximized; therefore, it is set to be 512 μm considering that it is limited by the spring deflection. Concerning the finger width (W_f), it is selected to be 7 μm which ensures proper operation of the converter [19].

Further, the shuttle mass length (L_m) should be increased; however, it is hindered by the spring and the converter dimensions. The optimal values for L_m and W_m are found to be 1 cm by 0.3 cm, respectively [19]. The dielectric distance (d) is assumed to be 50 μm to reduce the stray capacitance [43].

3. Main Governing Equations of the Electrostatic MEMS Converter

In this section, the main analytical equations which govern the converter performance are illustrated. Based on Figure 1, during the input vibration, the converter movable combs and spring move in the lateral direction. The capacitance changes due to the change of the dielectric gap between the combs drive fingers. The converter output power is given by Equation (3) [42,44].

$$P_{out} = 2f_0E \quad (3)$$

where P_{out} is the output power of the converter, E_{useful} is the useful energy per cycle and f_0 is the driving frequency of the input vibration source, which is also the converter resonant frequency. The converter is designed to operate based on the source of the input vibration taken from a gas turbine. Thus, the converter can be used in several different modes in critical industries such as power generation, oil and gas, process plants, aviation, as well domestic and smaller related applications [45,46].

In Equation (3), the factor of 2 is added to represent both the converter charging and discharging operations for each vibrational cycle [42,44]. The useful energy per cycle from the converter is given by Equation (4),

$$E_{useful} = \frac{1}{2}(C_{min}V_{max}^2 - C_{max}V_{min}^2) \quad (4)$$

where V_{max} is the maximum voltage, which is one of the basic key factors of the vibration energy harvesting system [19,33], it is determined by the converter and its power conditioning circuits. It has two limiting factors, the breakdown voltage of the power conditioning circuit, MOSFET switches, and the breakdown voltage of the converter. In this work, the 0.35 μm CMOS technology is used for designing the power conditioning circuit switches.

From such a technology file, the breakdown voltage for the power MOS transistors is equal to 18 V. Thus, V_{max} must be less than 18 V. For the design safety, V_{max} is assumed to be half of the power switches breakdown voltage, i.e., 9 V [47].

Furthermore, V_{max} must be less than the converter breakdown voltage, which is determined by the breakdown of the air existing between the converter fingers. Thus, the converter’s maximum electric field caused by V_{max} has to be less than the breakdown electric field of the air, which is 3×10^6 V/m [48].

To be able to determine the optimum value of V_{max} , two fingers of the converter are simulated using the MATLAB PDE toolbox. The maximum electric field, E_{max} , between two fingers of the converter is simulated at different input voltage (V_{ip}), 2, 4, 6, 8, 10 V. The optimum V_{max} is determined based on the conditions discussed herein. Figure 2 represents the electric field distribution and the maximum electric field (E_{max}) between two fingers of the converter for different input voltages. It is obvious that at V_{ip} equals 10 V, E_{max} is found to be 2×10^6 V/m, which is considered a risky value as it is close to the air breakdown electric field. Thus, to achieve a safer design, the optimum V_{max} must be set to 8 V, at which the maximum electric field (E_{max}) between the converter fingers is 1.6×10^6 V/m, which guarantees a safe design. Such a design value of the optimum V_{max} also satisfies the safe design concerning the breakdown voltage of the converter power conditioning circuit power switches [47]. Figure 3 represents E_{max} between the converter fingers at different input voltages. The figure highlights that at the optimum V_{max} , which is 8 V, E_{max} is 1.6×10^6 V/m which promotes the converter design.

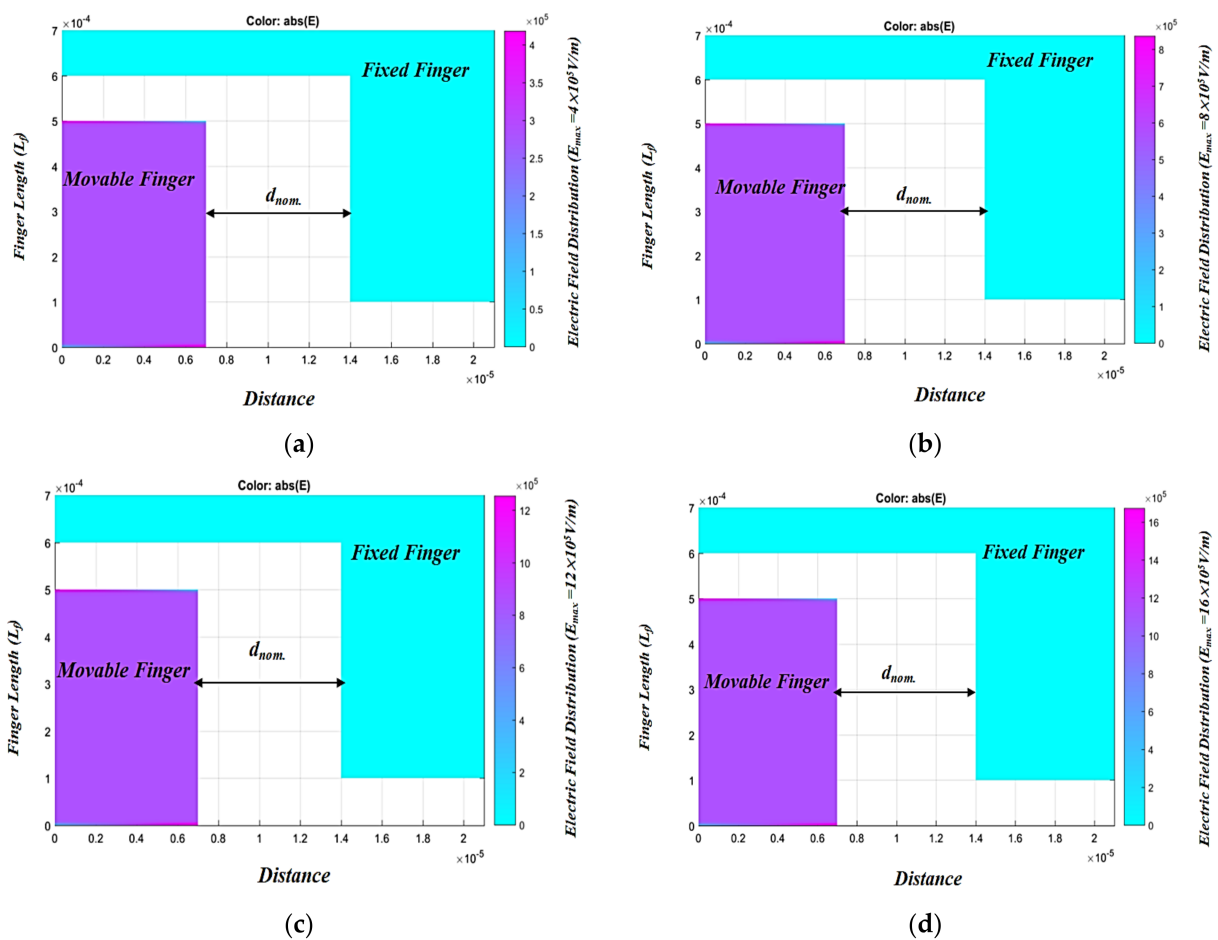


Figure 2. Cont.

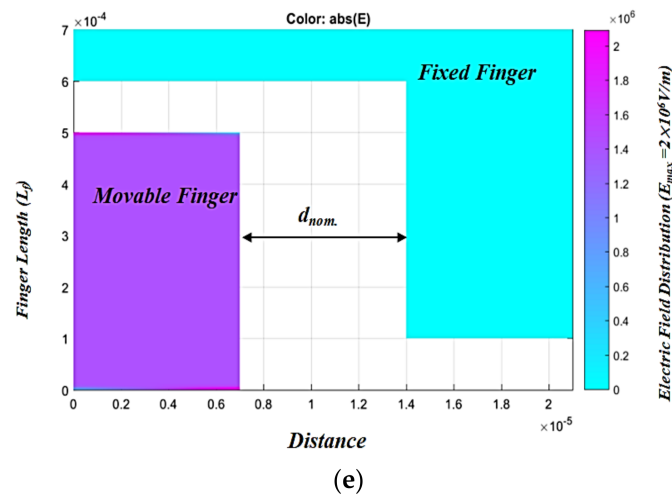


Figure 2. Electric field distribution between the converter fingers at different input voltage, V_{ip} (a) $V_{ip} = 2$ V, (b) $V_{ip} = 4$ V, (c) $V_{ip} = 6$ V, (d) $V_{ip} = 8$ V, and (e) $V_{ip} = 10$ V.

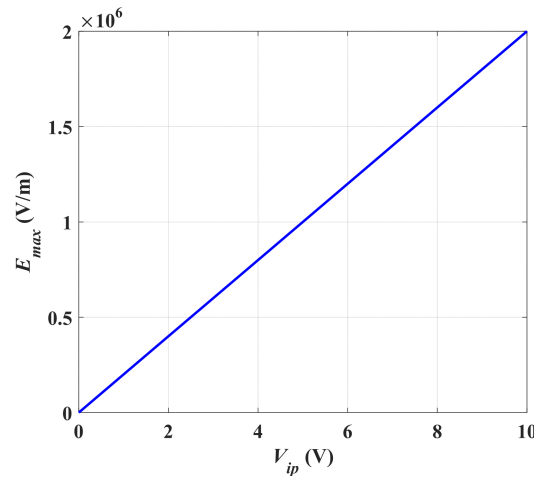


Figure 3. E_{max} between the converter fingers at different V_{ip} .

Referring to Equation (4), V_{min} is the converter’s initial voltage that exists on the converter at the beginning of each input vibration cycle to start the conversion operation. A reservoir capacitor is used to satisfy such an important requirement, as will be explained in the coming sections. In this work, the converter operation was based on the charge constrained technique which has the advantage of using one single initial voltage source to start the operation and satisfying that $V_{min} \ll V_{max}$ [33].

Thus, only one single charge source is needed to begin the process, and its value was less than V_{max} [33]. Based on the charge constrained conversion technique, Q was the charge placed on the converter fingers while its capacitance was at a maximum value. When the fingers are separated apart, the capacitance decreases until it reaches C_{min} while the voltage increases to V_{max} . Q is held constant according to the charge constrained conversion technique [33], where it is expressed by Equation (5),

$$Q = C_{max} V_{min} = C_{min} V_{max} \tag{5}$$

By substituting Equation (5) into Equation (4), E_{useful} is expressed by Equation (6)

$$E_{useful} = \frac{1}{2} \left(\frac{Q^2}{C_{min}} - \frac{Q^2}{C_{max}} \right) \tag{6}$$

By combining Equations (3) and (6), the final expression for the converter output power is given by Equation (7):

$$P_{out} = f_0 \left(\frac{Q^2}{C_{min}} \right) (1 - \alpha) \quad (7)$$

where $\alpha = C_{min}/C_{max}$. Based on Equation (7), the converter output power could be increased by increasing its C_{max} ; thus, the factor α will be decreased. Further, the converter output power could be increased by increasing the charge Q .

Next, by substituting Q from Equation (5) in Equation (7), the converter output power final expressed was given by Equation (8)

$$P_{out} = C_{min} V_{max}^2 (1 - \alpha) f_0 \quad (8)$$

To calculate the output power (P_{out}) of the converter according to the case study used in this work, recalling Table 1, C_{min} and C_{max} were calculated to be 8.8 nF and 0.6 nF, respectively. The value of α was calculated to be 0.07. Substituting V_{max} , f_0 , and α in (8), the maximum calculated P_{out} for the used case study is found to be 0.09 mW.

Now, in order to improve the converter output power, we propose the deposition of a thin layer of a high dielectric constant material, tantalum pentoxide (Ta_2O_5), on the converter comb drive fixed and movable fingers. Such deposition increases the converter's overall capacitances resulting in increasing the converter output power. Moreover, the deposited Ta_2O_5 acts as electrical stoppers which overcome the short circuit condition of the converter when its fingers come together. Figure 4 shows a simplified demonstration of the converter fixed and movable fingers with the deposition of the Ta_2O_5 thin layer.

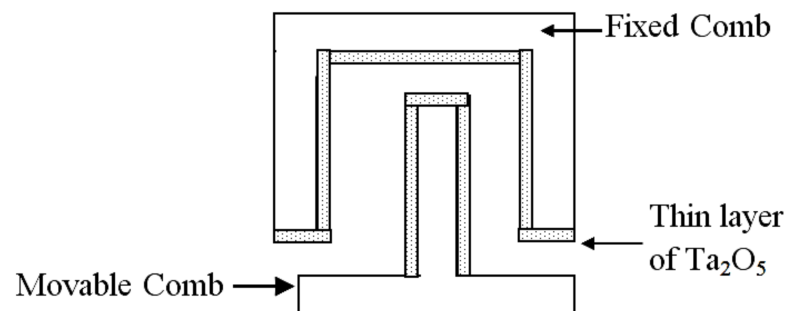


Figure 4. Demonstration of the converter fingers with the deposition of Ta_2O_5 .

The Ta_2O_5 material was selected for this case study as it has remarkable electrical and dielectric properties. It acts as an electrical insulator that has a high dielectric constant in the range of 25 to 35 [49]. The value of the Ta_2O_5 dielectric constant was set to the minimum value of 25 as a worst-case design for the required deposited thickness (d_{min}), which is 0.25 μm . This thickness was large enough to avoid the leakage problem that may occur when the dielectric materials layer thickness is in the range of nm [49–51]. The converter output power, P_{out} , was recalculated based on the effect of depositing the Ta_2O_5 . It became 2.3 mW. Figure 5 shows the converter output power in the two different cases, with and without the deposition of Ta_2O_5 on the converter fingers sidewalls. It is clear that the output power increased in the case of deposition. In the coming sections, the values of the enhanced converter capacitances with depositing Ta_2O_5 , will be used in the validation and evaluation of the behavioral circuit model.

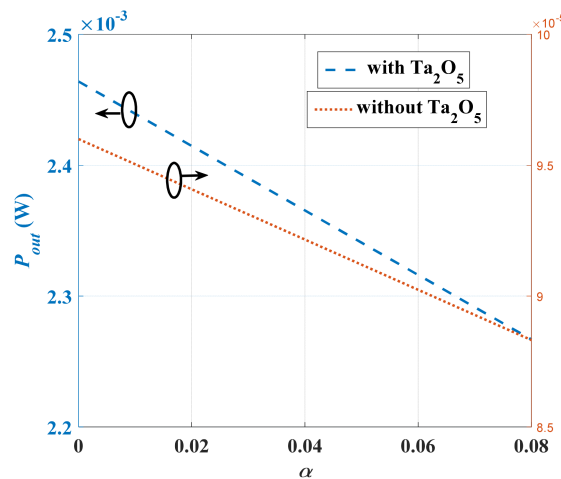


Figure 5. P_{out} versus α at two different cases (with and without the deposition of Ta_2O_5).

4. Proposed Behavioral Circuit Model of the Electrostatic MEMS Converter

In this section, our proposed behavioral circuit model [38–40] of the electrostatic MEMS converter is reinvestigated based on its capacitance variations with respect to the input displacement, x , caused by the vibration signal. Firstly, the converter behavior based on its C – x curve is qualitatively illustrated. Secondly, the converter proposed behavioral circuit model is presented. Finally, the vibration energy harvesting system block diagram, which contains the converter model with its assisted circuit, is explained.

4.1. Qualitative Analysis of the Electrostatic MEMS Converter Behavior Based on Its C – x Curve

In this subsection, the electrostatic MEMS converter behavior is qualitatively illustrated based on its C – x curve. Figure 6a,b demonstrate two fingers of the converter with the input displacement (x) caused by the input vibration signal and the converter C – x curve, respectively.

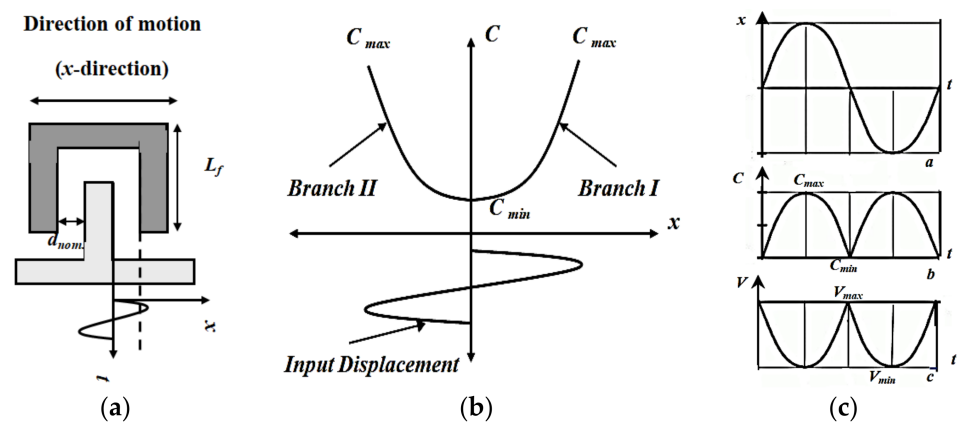


Figure 6. Qualitative analysis of the converter behavior (a) The converter two fingers representation, (b) The converter C – x curve, and (c) The input displacement (x), changes in capacitance and converter output voltage.

To explain the converter behavior based on its C – x curve, from Figure 6a,b, assume that the converter starts moving from its rest position at d_{nom} . (C_{min}). When the input displacement (x) increases in the positive x -direction at which the converter fingers move to the right, d_{nom} decreases to d_{min} , and the converter capacitance increases till it reaches C_{max} . Such an operation requires a quarter cycle of the input displacement. Then, when the input displacement decreases to complete the positive half cycle, the fingers move from d_{min} to d_{nom} . Thus, the converter capacitance decreases from C_{max} to C_{min} , which also requires another quarter cycle of the input displacement. This operation is represented by

branch I in Figure 6b. Thus, branch I gives a half cycle of the input displacement. From Figure 6b, branch II of the converter C - x curve is presented by moving the fingers from the rest position, d_{nom} , and C_{min} , in the negative x -direction to the left. It moves from C_{min} to C_{max} and then returns from C_{max} to C_{min} . It is clear that the MEMS converter operation is repeated twice during one complete cycle of the input vibration signal. Further, Figure 6c demonstrates the converter capacitance and voltage variations with respect to the input displacement caused by the input vibration signal. As mentioned in the previous section that the charge constrained technique is used in this work; the converter output voltage is inversely proportional to its capacitance variation, as displayed in Figure 6c.

4.2. Behavioral Circuit Model of the Enhanced Electrostatic MEMS Converter

In this subsection, based on the qualitative analysis of the converter behavior presented in the previous subsection, the converter behavioral circuit model is illustrated. In this model, a sampling of the converter C - x curve using both its C_{max} and C_{min} is performed. Figure 7 demonstrates the converter behavioral circuit model. The model is built up based on two types of circuit elements. The first type is the circuit elements which are based on the converter design, C_{max} and C_{min} . The second type is the elements that are necessary for accurately representing the converter behavior with respect to the input vibration signal, L_1 , I , S_1 , and S_2 . The values of C_{max} and C_{min} with the deposition of Ta_2O_5 are used, namely $0.22 \mu\text{F}$ and 15.4 nF . The coil, L_1 , is used as a charge pump technique. It is the model circuit element that is responsible for the charge transfer operation from C_{max} to C_{min} . The designed value of L_1 will be discussed in the coming section. Switches S_1 and S_2 are used to complete the charge transfer operation from C_{max} to C_{min} through L_1 . The current source, I , is used to represent the work undertaken by the converter to convert the input vibration signal into electricity.

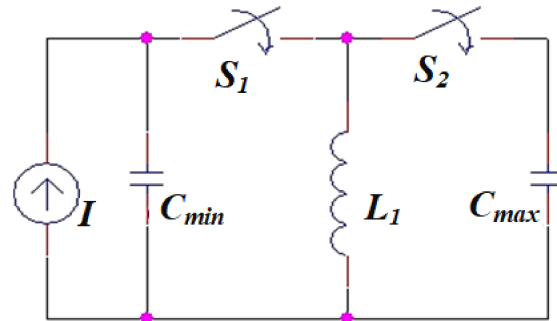


Figure 7. The behavioral circuit model of the electrostatic MEMS converter.

Figure 8 [38–40] demonstrates the block diagram of the vibration energy harvesting system which is required for reinvestigating the proposed model. This diagram will be utilized for the validation and evaluation of the converter behavioral circuit model. The converter model with its assisted circuit, the power conditioning circuit, is illustrated. This circuit is important for completing the converter operation [33].

Thus, the validation and evaluation of the converter behavioral circuit model will be accomplished through the model interaction with its accompanied circuit. Moreover, the required pulses which control the converter operation will be accurately determined.

As shown in Figure 8, a reservoir capacitor, C_{res} , must be used to give the initial charge for the electrostatic MEMS converter at the beginning of each input vibration cycle. Thus, it is considered the system supply. Moreover, when the converter exerts work to convert the input mechanical vibration signal into electricity, C_{res} stores the converted energy at the end of each input vibration cycle. So, it acts as a storage element. The value of C_{res} must be greater than the converter's maximum capacitance to fulfill its required operation as the system supply and storage element [33]. In this work, the value of C_{res} was assumed to be $22 \mu\text{F}$ which was sufficient for achieving its required operation, as illustrated in the coming section.

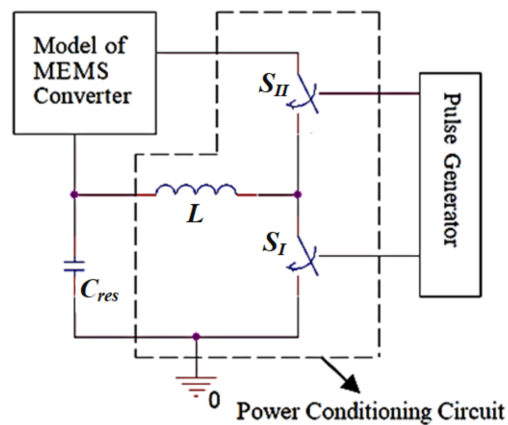


Figure 8. The block diagram for the vibration energy harvesting system.

Based on the normal operation of any capacitor, if the converter charges directly from C_{res} , it will charge by only half of its stored energy. Thus, half of the converted output power will be lost [52]. The coil, L , which is shown in Figure 8, is used to overcome this issue. It acts concurrently as a charge storage and transfer element. At the beginning of the input vibration cycle, L charges from C_{res} . So, it stores the charge till it reaches the required value to be transferred to the converter as an initial charge without any leakage. In our simulation, L was assumed to be 45 μH . This value was required for achieving the resonant frequency with C_{max} at the vibration frequency. Thus, the inductor can discharge in a quarter cycle of the input vibration. This means that the efficient charge transfer operation through the system could be achieved, as explained in the coming section.

The power switches S_I and S_{II} are essential for completing the charge transfer operation through the overall system. In this work, the controlling pulses of S_I and S_{II} operations are generated from a pulse generator. The specifications of such pulses, which are responsible for controlling the whole charge transfer operation through the system, are accurately illustrated and determined in the coming section. The design of the converter controlling circuit based on such specifications can be easily achieved.

5. Validation and Evaluation of the Electrostatic MEMS Converter Behavioral Circuit Model

In this section, the converter behavioral circuit model will be investigated through the interaction of the model with the power conditioning circuit explained in the previous section. Firstly, the converter model is qualitatively validated by illustrating the charge transfer operation between system components. Secondly, the proposed model is quantitatively evaluated by simulating its interaction with the power condition circuit. Finally, the required controlling pulses for the converter operation are accurately specified.

5.1. Qualitative Validation of the Converter Model

Figure 9a demonstrates the converter behavioral circuit model with its power conditioning circuit. As explained in the previous section, the controlling pulses are assumed to be generated from a pulse generator. Thus, the specifications of the required controlling pulses for the converter operation will be determined based on the model interaction with the power conditioning circuit. Some switches must be added to Figure 9a to complete the interaction between the converter model and the power conditioning circuit based on the controlling pulses. Figure 9b demonstrates the final circuit with all of the necessary added circuit elements used for validating and evaluating the converter model [38–40].

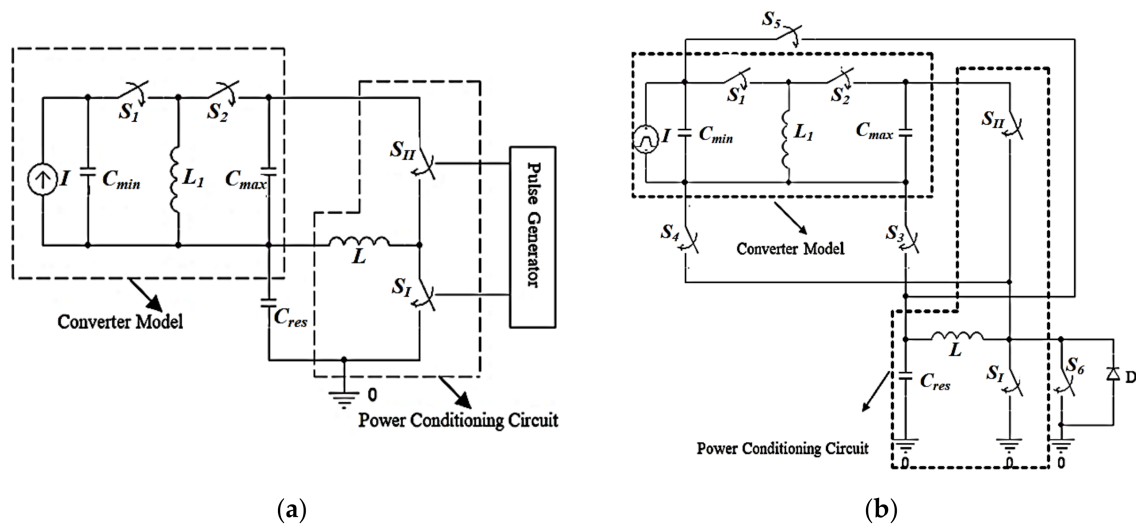


Figure 9. Demonstration of the converter behavioral circuit model with its power conditioning circuit (a) Converter behavioral circuit model with its power conditioning circuit, and (b) Final circuit with all the necessary added elements.

To be able to validate the converter model qualitatively, the required transitions between the model and C_{res} , which completely represent the vibration energy harvesting system operation, must be illustrated. Such transitions are based on the required controlling pulses for each switch included in Figure 9b. Figure 10 demonstrates the required stages for completing the operation of the vibration energy harvesting system.

There are three stages required for completing such an operation. The first stage is the charging of the converter from the system supply, C_{res} , by V_{min} when its capacitance is at C_{max} at the beginning of the input vibration cycle. Referring to Figure 9b, such a stage is carried out by charging the converter with V_{min} at C_{max} from C_{res} through L . S_I , S_{II} , and S_3 are responsible for such operation. Figure 10a demonstrates the controlling pulses of the switches, S_I , S_{II} , and S_3 , along with the charge transfer operations required for the first stage. It is obvious that L is charging by the converter initial charge from C_{res} when S_I is on, which is controlled by Pulse 1, P_1 . The amount of the converter required initial charge is determined based on the pulse width of P_1 , PW_1 . Then, L discharges in C_{max} and C_{max} charges to V_{min} from L when S_{II} and S_3 are on, which is controlled by pulse 2, P_2 .

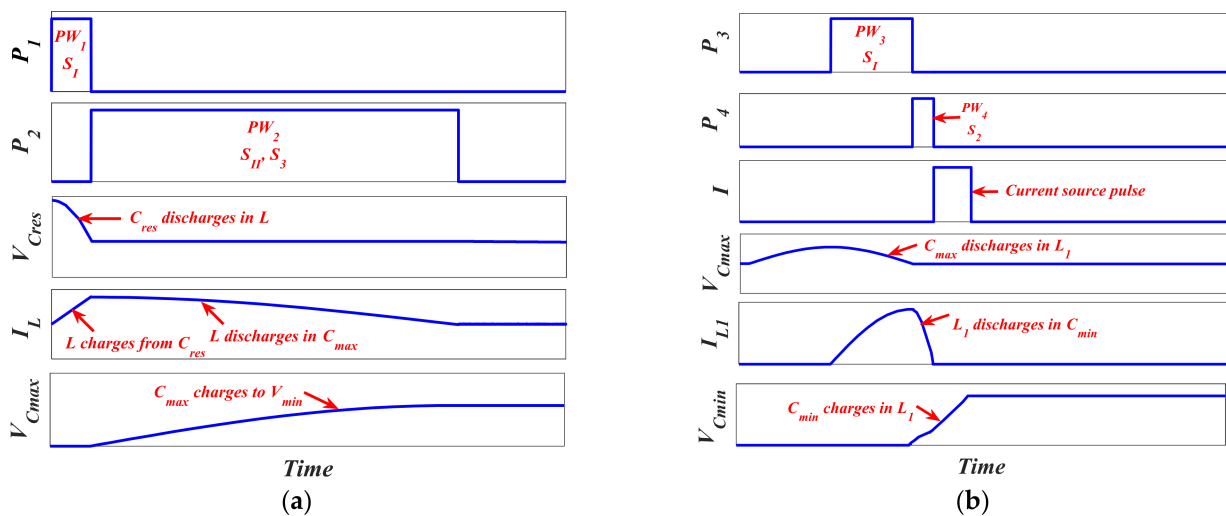


Figure 10. Cont.

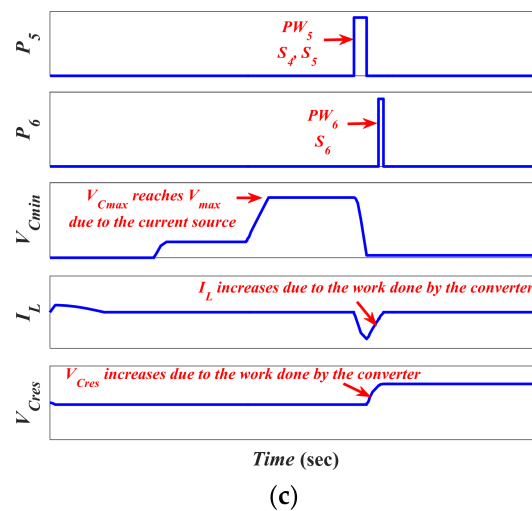


Figure 10. The three stages of the vibration energy harvesting system operation (a) The first stage, (b) The second stage, and (c) The third stage.

The second stage is the conversion of the input vibration signal into electricity using the converter model. Recalling the converter C – x curve in Figure 6b, firstly, the converter capacitance must decrease from C_{max} to C_{min} . Thus, its voltage must increase from V_{min} to V_{max} . The current source I is added to complete the charging of C_{min} to V_{max} . Thus, it is used to represent the converter exerted work through the conversion operation. S_1 and S_2 are responsible for such operation, as will be explained in detail in the coming section. Figure 10b demonstrates the switches controlling pulses along with the charge transfer operations required for the second stage. It is clear that, during pulse 3, P_3 , C_{max} discharges in L_1 through S_1 . Then L_1 charges C_{min} to V_{Cmin} during pulse 4, P_4 , through S_2 . Finally, the current source, I , complete the charging of C_{min} till V_{max} .

The third and final stage is the transfer of the gained energy caused by the conversion operation from the converter to the system storage element. Such an operation is carried out using L , S_4 , S_5 , and S_6 . Figure 10c demonstrates such a stage. As shown in the figure, L charges from C_{min} through pulse 5, P_5 , when S_4 and S_5 are on. Then C_{res} charges from L by the gained energy from the conversion operation through pulse 6, P_6 when S_6 is on. The diode, D , is added as system protection and to complete the transfer operation.

5.2. The Quantitative Evaluation of the Converter Model

In this subsection, the converter model operation is quantitatively evaluated using the OrCAD simulator. The essential three stages required to accurately represent the vibration energy harvesting system operation with all the required details are illustrated. The detailed operation with the accurate specification of each controlling pulse required for controlling switches operation during each transition is illustrated. Finally, the specifications of the converter operation controlling pulses are precisely determined. Moreover, the voltage of C_{res} at the beginning and the end of the input vibration cycle is simulated and illustrated.

5.2.1. Charging the MEMS Converter with the Initial Charge

In this subsection, the first stage of the vibration energy harvesting operation is illustrated. Figure 11 represents the simulation results for such stage by using OrCAD 16.6; assuming that the electrostatic MEMS converter capacitance is at C_{max} . At the beginning of the input vibration cycle, the converter must be charged with the initial charge to start the conversion operation. C_{res} , which acts as the system supply, is responsible for charging the converter with the required initial charge. Thus, the converter needs to be charged with a minimum voltage, V_{min} , from C_{res} . Referring to Figure 10, as mentioned in the previous sections, L is used as a charge storage element to save the losses which occur from the direct charge of the converter from C_{res} . Thus, it stores from C_{res} the required energy for charging

the converter with V_{min} . This charge transfer operation between L and C_{res} is controlled by S_I . The specification of S_I controlling pulse is responsible for limiting the charge transfer from C_{res} to L with the value of V_{min} .

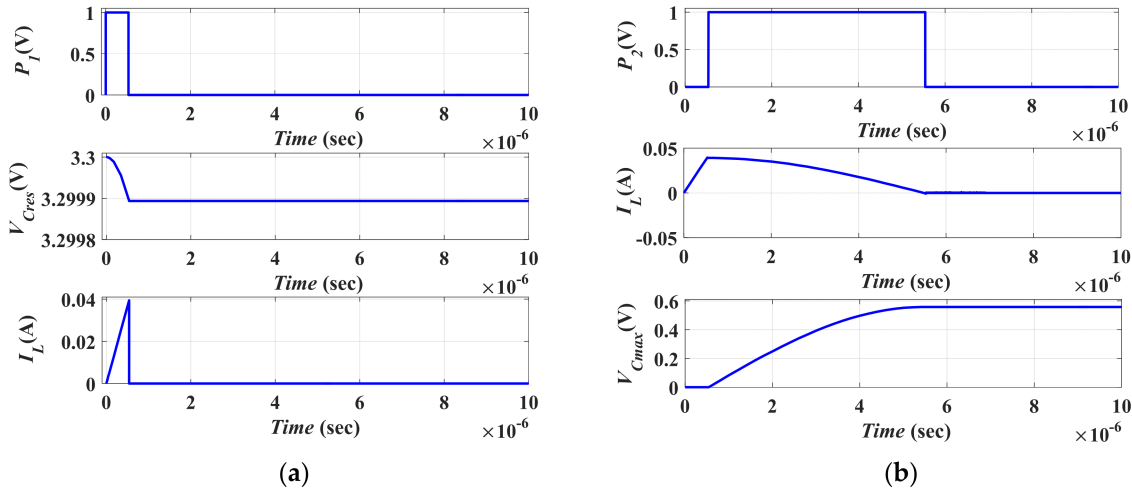


Figure 11. The first stage simulation results (a) The charging operation of L from C_{res} , and (b) The Simulation result of P_2 , and the voltage on C_{max} and I_L .

To calculate V_{min} , based on the charge constrained conversion operation [33], the charge (Q) will be constant during the transfer operation. Thus, V_{min} is determined by referring to Equation (5). Knowing that $C_{max} = 0.22 \mu\text{F}$, $C_{min} = 15.4 \text{ nF}$, and $V_{max} = 8 \text{ V}$, then V_{min} is 0.56 V. Further, to determine the specifications of the controlling pulse P_1 , which controls S_I operation, the pulse width of P_1 must be calculated from the maximum current required to charge C_{max} to V_{min} . It means that when the charge is transferred from L to C_{max} , the kinetic energy on L is changed to potential energy on the capacitor, C_{max} . As both C_{max} potential energy and L kinetic energy must be equal, as indicated in Equation (9),

$$C_{max}V_{min}^2 = LI_{Lmax}^2 \tag{9}$$

Given the following values $V_{min} = 0.56 \text{ V}$, $C_{max} = 0.22 \mu\text{F}$, $L = 45 \mu\text{H}$, I_{Lmax} is found to be 39 mA.

To determine the pulse width of P_1 , which controls the operation of S_I , PW_1 , L must be charged from C_{res} by a maximum current. At the end of the charging cycle, the coil voltage, V_L , must reach V_{supply} , which is the voltage of C_{res} . Thus, PW_1 is calculated from Equation (10),

$$V_L = (LI_{Lmax})/PW_1 \tag{10}$$

In this simulation, $V_{C_{res}}$ was assumed to be 3.3 V which is the supply limiting voltage of the 0.35 μm technology used for the power switches [47]. Thus, PW_1 was calculated to be 0.53 μs. To let L completely charge to the required maximum current, PW_1 was set to be 0.537 μs. Figure 11a illustrates the simulation result of charging L from C_{res} by the initial charge required to be placed on the converter at the beginning of the input vibration cycle.

It is clear that the simulated value of I_{Lmax} is 39.027 mA which agrees with the calculated value. In addition, $V_{C_{res}}$ decreases to 3.2999 V, which clarifies that C_{res} acts as a supply for the system. Then, the stored energy on L is transferred to charge C_{max} by V_{min} through S_{II} . As L must be completely discharged in C_{max} , V_L must reach zero volts. This operation requires a quarter of the resonant period of the $L_{C_{max}}$ resonant circuit. Thus, the required pulse width of P_2 , PW_2 , which is required to control the operation of S_{II} and S_3 , is calculated from Equation (11)

$$PW_2 = \frac{T_{res}}{4} \tag{11}$$

where, T_{res} is the resonance time constant. So, the resonance frequency (f_{res}) could be calculated from

$$f_{res} = \frac{1}{T_{res}} = \frac{1}{2\pi\sqrt{LC_{max}}} \tag{12}$$

For $L = 45 \mu\text{H}$ and $C_{max} = 0.22 \mu\text{F}$, $f_{res} = 50 \text{ MHz}$ and thus, $PW_2 = 5 \mu\text{s}$. To avoid the over or under discharging of C_{max} from the coil, a slight delay must exist between P_1 and P_2 . Thus, PW_2 is assumed to be $0.538 \mu\text{s}$. Figure 11b illustrates the simulation result of S_{II} and S_3 controlling pulse, P_2 , and the voltage on C_{max} and the current I_L . From the figure, it is obvious that the voltage on C_{max} is 0.552 V which agrees with the calculated value. Moreover, I_L decreases to 0 A at the end of PW_2 . It means that L transfers all the required initial charges to C_{max} .

5.2.2. Vibration Energy Conversion Representation by the Converter Model

Figure 12 shows the second stage of the vibration energy harvesting system operation. The conversion of the vibration energy by using the converter model is illustrated. To complete the conversion operation, recalling Figure 6b, the converter capacitance must change from C_{max} , which has V_{min} , to C_{min} , which has V_{max} . Then the converter capacitance must change again from C_{min} to C_{max} to complete the positive half cycle of the input vibration. Such a process is carried out by the converter model as follows. Firstly, the initial charge on C_{max} must be transferred to C_{min} through L_1 . Thus, L_1 must charge to the maximum current, I_{L1max} , from C_{max} through S_1 .

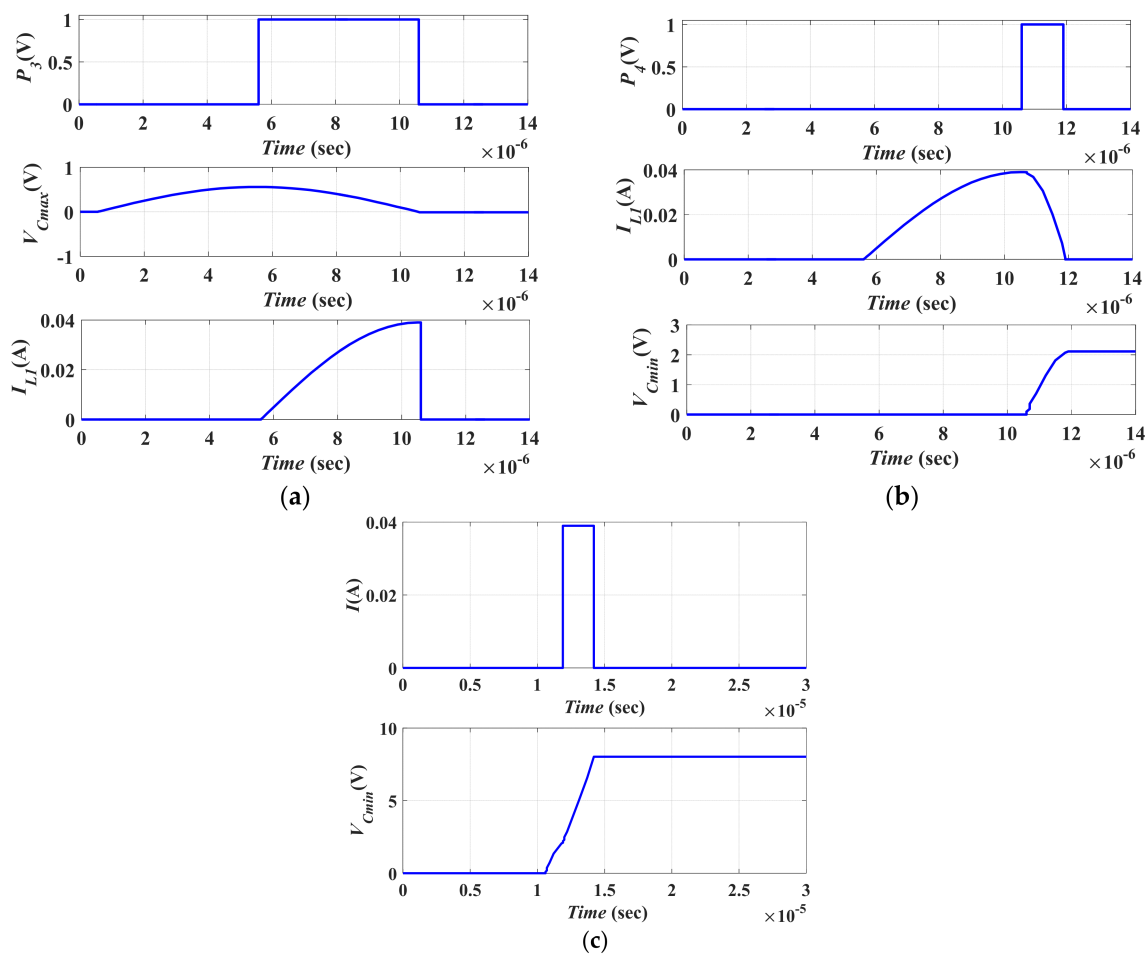


Figure 12. The second stage simulation results (a) The Simulation result of P_3 , and the charging current of and L_1 , (b) Charging of C_{min} from L_1 during PW_4 through S_2 , and (c) Boosting V_{Cmin} to V_{max} by the effect of I .

By charging L_1 from C_{max} , the coil potential energy is transferred to kinetic energy, which is expressed by Equation (13)

$$C_{max} V_{min}^2 = L_1 I_{L1max}^2 \tag{13}$$

Using the values: $C_{max} = 0.22 \mu\text{F}$, $V_{min} = 0.56 \text{ V}$, and $L_1 = 45 \mu\text{H}$. I_{L1max} is found to be 39 mA.

Theoretically, the pulse width of P_3 , PW_3 , which controls the operation of S_1 , must equal the pulse width of P_2 as L_1 equals L . Slight delay must be added between P_2 and P_3 to avoid the overlap between the operations. Thus, $PW_3 = 5 \mu\text{s}$. Figure 12a shows the charging of L_1 during PW_3 . It is clear that I_{L1max} is 39 mA, which agrees with the calculated value. Then, C_{min} must be charged by V_{Cmin} by transferring the charge on L_1 to C_{min} through S_2 . Thus, the kinetic energy of L_1 is transformed to potential energy on C_{min} as expressed in Equation (14)

$$C_{min} V_{Cmin}^2 = L_1 I_{L1max}^2 \tag{14}$$

Substituting $C_{min} = 15.4 \text{ nF}$, $L_1 = 45 \mu\text{H}$, and $I_{L1max} = 39 \text{ mA}$ in Equation (14), V_{Cmin} was found to be 2.1 V.

Next, the pulse width of P_4 , PW_4 , required to control the operation of S_2 , was calculated from Equation (11) to be $PW_4 = (\frac{1}{4}) T_{res} = 1.3 \mu\text{s}$ given $L_1 = 45 \mu\text{H}$ and $C_{min} = 15.4 \text{ nF}$. The resonance frequency was calculated based on the following equation,

$$f_{res} = \frac{1}{T_{res}} = \frac{1}{2\pi\sqrt{L_1 C_{min}}} \tag{15}$$

In this step, L_1 must be directly discharged in C_{min} ; thus, there is no need for inserting a delay between P_3 and P_4 . If any delay exists, there will be no path for L_1 to discharge in C_{min} . Figure 12b shows the charging of C_{min} from L_1 during PW_4 through S_2 .

It is clear that V_{Cmin} was 2.1 V which agreed with the calculated value. To enable the converter to complete the conversion operation, V_{Cmin} must reach V_{max} , which was 8 V in this work. Thus, recalling Figure 7, a current source (I) was added to the converter model. This added source was responsible for representing the work undertaken by the converter, which was required to boost V_{Cmin} to V_{max} when the converter capacitances changed from C_{max} to C_{min} . Both magnitude and pulse width of the current source, I , were calculated based on the extra charge, Q_{extra} , required to boost V_{Cmin} to V_{max} . Q_{extra} was calculated from Equation (16)

$$Q_{extra} = \Delta V_{Cmin} C_{min} = (V_{Cmin(final)} - V_{Cmin(initial)}) C_{min} \tag{16}$$

Substituting in Equation (16) by: $V_{Cmin(initial)} = 2.1 \text{ V}$, $V_{Cmin(final)} = V_{max} = 8 \text{ V}$ and $C_{min} = 15.4 \text{ nF}$, thus Q_{extra} is calculated to be 90.86 nC. As $Q_{extra} = I_{max} t$, where I_{max} is the peak of the current source, and t is its pulse width. The peak current I_{max} was assumed to have the maximum current of L and L_1 , which was 39 mA. From Figure 12c, it is apparent that the voltage on C_{min} increases from V_{Cmin} , 2.1 V, to V_{max} , because of the current source, as explained before.

5.2.3. Transfer the Gained Energy from Conversion Operation back to C_{res}

In this subsection, the final stage required to completely represent the vibration energy conversion operation is illustrated. At the end of the input vibration cycle, the gained energy from the conversion operation is transferred to the system storage element, C_{res} , through L . Firstly, the gained energy was transferred to L from C_{min} through PW_5 when S_4 and S_5 were ON. The discharging of C_{min} in L follows the same concept of discharging L_1 in C_{min} . Thus, the required pulse width of P_5 , PW_5 , for discharging C_{min} in L equals the pulse width of P_4 , PW_4 , which was 1.3 μs . By charging L from C_{min} , the potential energy was transferred to kinetic energy. So, following the same approach as before, one can find I_L to be 147.99 mA.

Figure 13a shows the discharging of C_{min} in L during PW_5 through S_4 and S_5 and the coil current, which agrees with the calculated value, 148 mA. Secondly, the gained energy which is stored in L is transferred to the system storage element, C_{res} . Thus, L discharges in C_{res} through P_6 when S_6 is on. Figure 13b shows the transferring of the gained energy from L to C_{res} . It is obvious that $V_{C_{res}}$ increases from 3.299 V to 3.305 V.

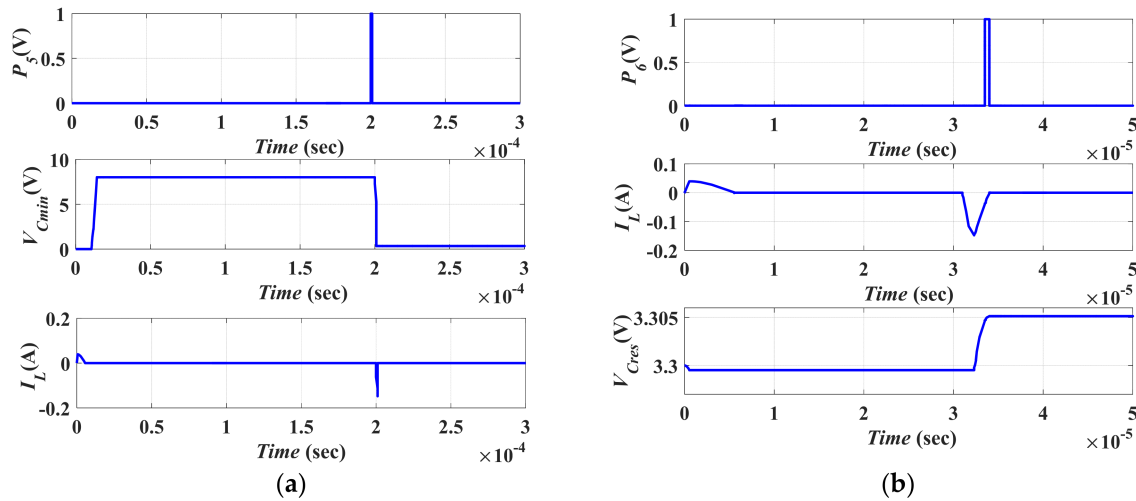


Figure 13. The third stage simulation results (a) The discharging of C_{min} in L during PW_5 through S_4 and S_5 , and (b) Transferring the gained energy from L to C_{res} during PW_6 .

It is important to calculate the gained energy caused by the conversion of the input vibration signal into an electric signal using the converter model. In order to calculate the gained energy by C_{res} from the conversion process, the initial voltage on C_{res} ($V_{initial}$) has to be specified. This is the voltage on C_{res} at the start of the input vibration cycle. In addition, the final voltage on C_{res} (V_{final}) has to be specified. This is the voltage on C_{res} at the end of the input vibration cycle. As the input vibration frequency in this study is 2.5 kHz, thus the input vibration cycle is 0.4 ms. From Figure 13b, it is clear that the values of the $V_{initial}$ and V_{final} are 3.299 V and 3.305 V, respectively. The gained energy by C_{res} is given by Equation (17)

$$E_{gained} = E_{final} - E_{initial} = C_{res} \Delta V_{C_{res}}^2 \tag{17}$$

Where $\Delta V_{C_{res}}^2$ is given by, $\Delta V_{C_{res}}^2 = V_{final}^2 - V_{initial}^2$, taking the previously listed value of C_{res} , E_{gained} is found to be 0.44 μ J. Moreover, the gained power by C_{res} from the system is given by Equation (18)

$$P_{gained} = 2fE_{gained} \tag{18}$$

Given $f = 2.5$ kHz, $E_{gained} = 0.44$ μ J, P_{gained} was found to be 2.2 mW which gives a good agreement with the calculated value of P_{out} from the converter, which was 2.3 mW.

Finally, Figure 14 illustrates the simulation of $V_{C_{res}}$ for multiple cycles of the input vibration signal. Such a figure emerges as the major contribution of C_{res} to the vibration energy harvesting system. It verifies that C_{res} acts as the system supply at the beginning of the input vibration cycle. Therefore, $V_{C_{res}}$ decreases by the value required initially to charge the converter. At the end of the input vibration cycle, C_{res} acts as the system storage element. So, $V_{C_{res}}$ increases by the value of the gained energy from the conversion operation.

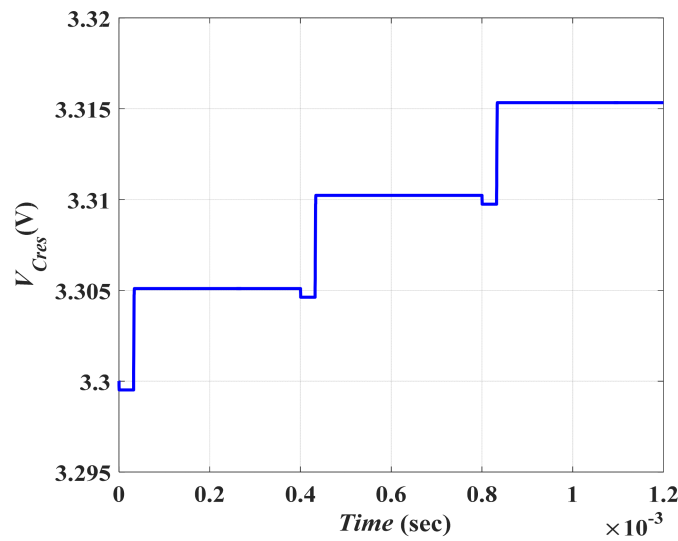


Figure 14. Variation of $V_{C_{res}}$ during multiple cycle of the input vibration signal.

The proposed behavioral circuit model is applied to a traditional simulated electrostatic in-plane gap closing MEMS converter from reference [20] and to another practically fabricated converter from reference [26] to provide a calibration study and to validate the accuracy of our presented model. The interaction between the model of the traditional converters and the system is simulated. Figure 15a,b show the simulation results of $V_{C_{res}}$, which is the main measurement of the system’s efficient performance during one cycle of the input vibration frequency for both cases.

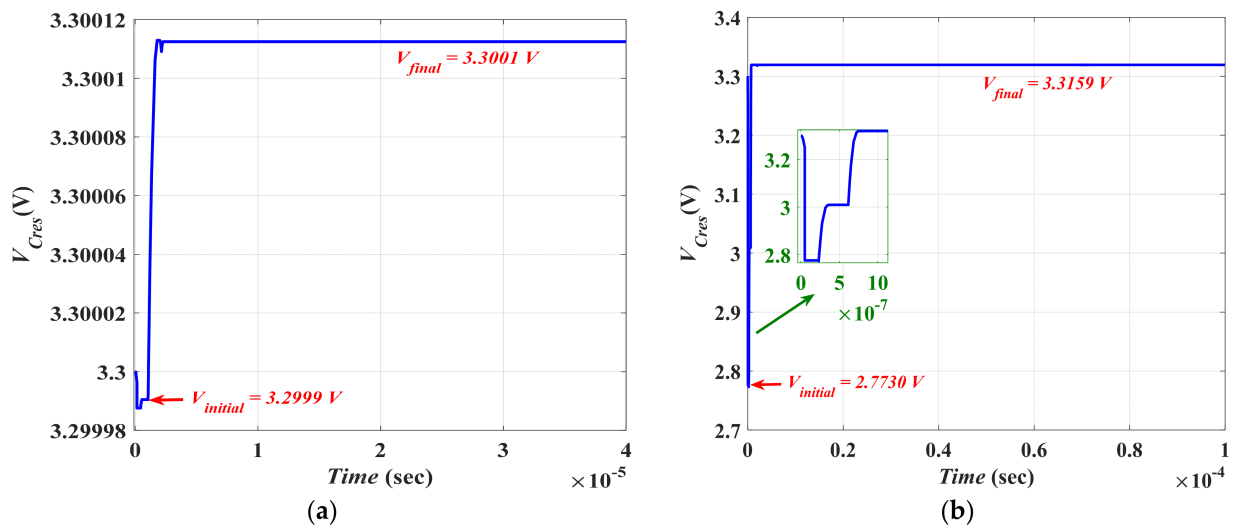


Figure 15. The reservoir capacitor voltage (a) for the simulated converter (b) for the fabricated converter.

From the simulation results, based on the value of the initial and final voltage on C_{res} and by using Equations (17) and (18), the gained energy and the output power from the system were calculated for both calibrated cases. Table 2 lists the main input parameters used in our simulation that were extracted from the published studies [20,26], while Table 3 presents a comparison between our used converter case study and both the simulated and fabricated converters. The relative absolute percentage error is also shown, indicating errors that are less than 10%.

Table 2. Input parameters of different designs of electrostatic MEMS converters. Also, our design input parameters are shown for comparison.

Input Parameters	REF [20]	REF [26]	Our Work
C_{max}	800 nF	290 pF	0.22 μ F
C_{min}	20 nF	40 pF	15.4 nF
V_{max}	100 V	10 V	8 V
f_o	120 Hz	250 Hz	2.5 kHz
C_{res}	200 nF	5 nF	22 μ F

Table 3. Comparison between output parameters of different studies and our model calculations showing the relative absolute percentage errors of results with respect to ours.

	E_{gained}	P_{gained}	Method
REF [20]	0.175 μ J	42 μ W	Analytical modeling
Our Model	0.189 μ J	45 μ W	Circuit simulation
$\Delta\xi$ (%)	8.00	7.14	
REF [26]	8.8 nJ	4.4 μ W	Experimental
Our Model	8.2 nJ	4.1 μ W	Circuit simulation
$\Delta\xi$ (%)	6.82	6.82	

6. Conclusions

To overcome the difficulty of fabricating the electrostatic MEMS converter due to the unavailability of fabrication facilities, we have investigated a modified behavioral circuit model for the MEMS converter based on its $C-x$ curve. Such a model has the advantage of being adaptive; thus, it can be applied to any MEMS converter system. Additionally, the model enables the implementation and testing of the MEMS converter along with the overall vibration energy harvesting system using commercially available off-shelf components. Thus, the designed converter performance can be cheaply tested and evaluated before going through the costly fabrication procedures.

Moreover, a proposed technique is presented for which the conventional in-plan gap-closing electrostatic MEMS converter performance is enhanced by depositing Ta_2O_5 on its sidewall fingers. The main equations which govern the converter performance are illustrated. One of the main basic key parameters of the vibration energy harvesting system is the maximum voltage V_{max} , which is thoroughly investigated. Based on the simulation results using the MATLAB PDE tool, the optimum V_{max} is found to be 8 V. Thus, the output power of the enhanced converter is calculated to be 2.3 mW which is considered an appreciable enhancement in comparison with recently cited work.

Next, the behavioral model is applied to the proposed enhanced structure. Firstly, the model is qualitatively validated by illustrating its behavior during the three essential stages required for successfully achieving the vibration energy conversion operation. Then, the model is quantitatively evaluated using the Orcad simulator. Based on the simulation results, the required controlling pulses for the converter operation are accurately specified, which gives the advantage of the ease of implementing the converter controlling circuit. Moreover, the simulation results emphasize that the generated output power from the converter model based on its interaction with the system shows a good agreement with the analytically calculated output power of the converter, 2.3 mW. Thus, the converter behavioral circuit model accurately accomplished the vibration energy conversion operation. Finally, the proposed behavioral circuit model is applied to traditional simulated and fabricated electrostatic in-plane gap closing MEMS converter to provide a calibration study and to validate the accuracy of our presented model; it gives good agreement with such cases; thus, the model accuracy is verified. In our future work, we intend to practically implement and test the proposed converter behavioral circuit model along with its power conditioning circuit. Furthermore, the system performance will be examined using different

loads. Moreover, the enhanced converter will be simulated by FEM under the MATLAB environment to optimize its technological, physical, and mechanical parameters to improve its performance.

Author Contributions: Conceptualization, M.S.S. (Mona S. Salem), A.Z. and M.S.S. (Marwa S. Salem); methodology, M.S.S. (Mona S. Salem), A.Z. and A.S.; validation and formal analysis, M.S.S. (Mona S. Salem), A.Z., M.A. and M.S.S. (Marwa S. Salem); Funding acquisition, M.S.S. (Mona S. Salem); Visualization, A.S., M.A. and A.Z.; investigation, All authors; writing—original draft preparation, M.S.S. (Mona S. Salem), A.S. and M.S.S. (Marwa S. Salem); writing—review and editing, All authors; supervision, A.Z., M.A., A.S. and M.S.S. (Marwa S. Salem) All authors have read and agreed to the published version of the manuscript.

Funding: This research received no external funding.

Institutional Review Board Statement: Not applicable.

Informed Consent Statement: Not applicable.

Data Availability Statement: No new data were created or analyzed in this study. Data sharing is not applicable to this article.

Conflicts of Interest: The authors declare no conflict of interest. The funders had no role in the design of the study; in the collection, analyses, or interpretation of data; in the writing of the manuscript, or in the decision to publish the results.

References

- Sullivan, J.L.; Gaines, L. *A Review of Battery Life-Cycle Analysis: State of Knowledge and Critical Needs*; Technical Report; Argonne National Lab (ANL): Argonne, IL, USA, 2010. [\[CrossRef\]](#)
- Paulo, J.; Gaspar, P.D. Review and future trend of energy harvesting methods for portable medical devices. In Proceedings of the World Congress on Engineering, London, UK, 30 June–2 July 2010.
- Shaikh, F.K.; Zeadally, S. Energy harvesting in wireless sensor networks: A comprehensive review. *Renew. Sustain. Energy Rev.* **2016**, *55*, 1041–1054. [\[CrossRef\]](#)
- Davidson, J.; Mo, C. Recent advances in energy harvesting technologies for structural health monitoring applications. *Recent Adv. Energy Harvest. Technol. Struct. Health Monit. Appl.* **2014**, *2014*, 410316. [\[CrossRef\]](#)
- Ng, C.H.; Lim, H.N.; Hayase, S.; Zainal, Z.; Huang, N.M. Photovoltaic performances of mono-and mixed-halide structures for perovskite solar cell: A review. *Renew. Sustain. Energy Rev.* **2018**, *90*, 248–274. [\[CrossRef\]](#)
- Yang, Y.; Wang, S.; Stein, P.; Xu, B.X.; Yang, T. Vibration based energy harvesting with a clamped piezoelectric circular diaphragm: Analysis and identification of optimal structural parameters. *Smart Mater. Struct.* **2017**, *26*, 045011. [\[CrossRef\]](#)
- Ando Junior, O.H.; Maran, A.L.O.; Henao, N.C. A review of the development and applications of thermoelectric microgenerators for energy harvesting. *Renew. Sustain. Energy Rev.* **2018**, *91*, 376–393. [\[CrossRef\]](#)
- Wang, H.; Jasim, A.; Chen, X. Energy harvesting technologies in roadway and bridge for different applications: A comprehensive review. *Appl. Energy* **2018**, *212*, 1083–1094. [\[CrossRef\]](#)
- Fang, S.; Fu, X.; Du, X.; Liao, W.H. A music-box-like extended rotational plucking energy harvester with multiple piezoelectric cantilevers. *Appl. Phys. Lett.* **2019**, *114*, 233902. [\[CrossRef\]](#)
- Jung, I.; Shin, Y.H.; Kim, S.; Choi, J.Y.; Kang, C.Y. Flexible piezoelectric polymer-based energy harvesting system for roadway applications. *Appl. Energy* **2017**, *197*, 222–229. [\[CrossRef\]](#)
- Tan, Q.; Fan, K.; Tao, K.; Zhao, L.; Cai, M. A two-degree-of-freedom string-driven rotor for efficient energy harvesting from ultra-low frequency excitations. *Energy* **2020**, *196*, 117107. [\[CrossRef\]](#)
- Tao, K.; Wu, J.; Tang, L.; Xia, X.; Lye, S.W.; Miao, J.; Hu, X. A novel two-degree-of-freedom MEMS electromagnetic vibration energy harvester. *J. Micromech. Microeng.* **2016**, *26*, 035020. [\[CrossRef\]](#)
- Naruse, Y.; Matsubara, N.; Mabuchi, K.; Izumi, M.; Suzuki, S. Electrostatic micro power generation from low-frequency vibration such as human motion. *J. Micromech. Microeng.* **2009**, *19*, 094002. [\[CrossRef\]](#)
- Arroyo, E.; Badel, A.; Formosa, F.; Wu, Y.; Qiu, J. Comparison of electromagnetic and piezoelectric vibration energy harvesters: Model and experiments. *Sens. Actuators A Phys.* **2012**, *183*, 148–156. [\[CrossRef\]](#)
- Beeby, S.P.; Wang, L.; Zhu, D.; Weddell, A.S.; Merrett, G.V.; Stark, B.; Szarka, G.; Al-Hashimi, B.M. A comparison of power output from linear and nonlinear kinetic energy harvesters using real vibration data. *Smart Mater. Struct.* **2013**, *22*, 075022. [\[CrossRef\]](#)
- Sojan, S.; Kulkarni, R.K. A Comprehensive Review of energy harvesting techniques and its potential applications. *Int. J. Comput. Appl.* **2016**, *139*, 14–19. [\[CrossRef\]](#)
- Zhang, Y.; Wang, T.; Luo, A.; Hu, Y.; Li, X.; Wang, F. Micro electrostatic energy harvester with both broad bandwidth and high normalized power density. *Appl. Energy* **2018**, *212*, 362–371. [\[CrossRef\]](#)

18. Sundriyal, P.; Bhattacharya, S. Energy harvesting techniques for powering wireless sensor networks in aircraft applications: A review. In *Sensors for Automotive and Aerospace Applications*; Springer: Singapore, 2019; pp. 55–76.
19. Meninger, S.; Miranda, J.M.; Chandrakasan, J.L.A.; Slocum, A.; Schmidt, M.; Amirtharajah, R. Vibration to electric energy conversion. *IEEE Trans. Very Large Scale Integr. (VLSI) Syst.* **2001**, *9*, 64–76. [[CrossRef](#)]
20. Roundy, S.; Wright, P.K.; Rabaey, J. A study of low level vibrations as a power source for wireless sensor nodes. *Comput. Commun.* **2003**, *26*, 1131–1144. [[CrossRef](#)]
21. Boisseau, S.; Despesse, G.; Seddik, B.A. *Electrostatic Conversion for Vibration Energy Harvesting, Small-Scale Energy Harvesting*, 5th ed.; Lallart, M., Ed.; LETI, CEA, Minatec Campus: Grenoble, France, 2012. [[CrossRef](#)]
22. Aljadiri, R.T.; Taha, L.Y.; Ivey, P. Electrostatic harvester for wind energy harvesting and wind speed remote sensing. In Proceedings of the 2015 IEEE 28th Canadian Conference on Electrical and Computer Engineering (CCECE), Halifax, NS, Canada, 3–6 May 2015. [[CrossRef](#)]
23. Taylor, S.G.; Park, G.; Farinholt, K.M.; Todd, M.D. Diagnostics for piezoelectric transducers under cyclic loads deployed for structural health monitoring applications. *Smart Mater. Struct.* **2013**, *22*, 025024. [[CrossRef](#)]
24. Elliott, A.D.T.; Miller, L.M.; Halvorsen, E.; Wright, P.K.; Mitcheson, P.D. Which is better, electrostatic or piezoelectric energy harvesting systems? *J. Phys. Conf. Ser.* **2015**, *660*, 012128. [[CrossRef](#)]
25. Aljadiri, R.T.; Taha, L.Y.; Ivey, P. Electrostatic Energy Harvesting Systems: A Better Understanding of Their Sustainability. *J. Clean. Energy Technol.* **2017**, *5*, 5. [[CrossRef](#)]
26. Guillemet, R.; Basset, P.; Galayko, D.; Marty, F.; Bourouina, T. Efficient inplane gapclosing MEMS electrostatic vibration energy harvester. *Power MEMS* **2012**, *2012*, 137–140.
27. Demirhan, G. Resonance-Based Mems Temperature Sensors for Temperature Compensation of Mems Capacitive Accelerometer. Master's Thesis, Middle East Technical University, Ankara, Turkey, 2016.
28. Hsieh, K.Y.; Chiu, J.; Lu, M.S.C. Development of CMOS micromachined capacitive squeeze-film pressure sensors. *IEEE Sens. J.* **2017**, *20*, 9698–9705. [[CrossRef](#)]
29. Algamili, A.S.; Khir, M.H.M.; Dennis, J.O.; Ahmed, A.Y.; Alabsi, S.S.; Hashwan, S.S.B.; Junaid, M.M. A review of actuation and sensing mechanisms in mems-based sensor devices. *Nanoscale Res. Lett.* **2021**, *16*, 16. [[CrossRef](#)]
30. Jeong, B.; Kim, M.O.; Lee, J.I.; Eun, Y.; Choi, J.; Kim, J. Development of MEMS multi-mode electrostatic energy harvester based on the SOI process. *Micromachines* **2017**, *8*, 51. [[CrossRef](#)]
31. Honma, H.; Mitsuya, H.; Hashiguchi, G.; Fujita, H.; Toshiyoshi, H. Improvement of energy conversion effectiveness and maximum output power of electrostatic induction-type MEMS energy harvesters by using symmetric comb-electrode structures. *J. Micromech. Microeng.* **2018**, *28*, 064005. [[CrossRef](#)]
32. Naito, Y.; Uenishi, K. Electrostatic MEMS vibration energy harvesters inside of tire treads. *Sensors* **2019**, *19*, 890. [[CrossRef](#)] [[PubMed](#)]
33. Karami, A. Study of Electrical Interfaces for Electrostatic Vibration Energy Harvesting. Ph.D. Thesis, Sorbonne Université, Paris, France, 2018.
34. Ryalat, M.; Salim Damiri, H.; ElMoaqet, H.; AlRabadi, I. An Improved Passivity-based Control of Electrostatic MEMS Device. *Micromachines* **2020**, *11*, 688. [[CrossRef](#)]
35. Hasan, M.H.; Abbasalipour, A.; Nikfarjam, H.; Pourkamali, S.; Emad-Un-Din, M.; Jafari, R.; Alsaleem, F. Exploiting pull-in/pull-out hysteresis in electrostatic MEMS sensor networks to realize a novel sensing continuous-time recurrent neural network. *Micromachines* **2021**, *12*, 268. [[CrossRef](#)]
36. Syms, R.; Bouchaala, A. Mechanical Synchronization of MEMS Electrostatically Driven Coupled Beam Filters. *Micromachines* **2021**, *12*, 1191. [[CrossRef](#)]
37. Chiu, Y.; Kuo, C.T.; Chu, Y.S. Design and fabrication of a micro electrostatic vibration-to-electricity energy converter. *arXiv* **2007**, arXiv:0711.3313. [[CrossRef](#)]
38. Salem, M.S.; Salem, M.S.; Zekry, A.A.; Ragai, H.F. Modeling of Q–V Diagram Using SPICE for Electrostatic MEMS Converter Found in Energy Scavenging Systems. *Appl. Mech. Mater.* **2013**, *313*, 967–970. [[CrossRef](#)]
39. Salem, M.S.; Salem, M.S.; Zekry, A.A.; Ragai, H.F. Design methodology and power conditioning circuit of vibration based MEMS converters for wireless sensor networks. In Proceedings of the 2005 International Conference on Information and Communication Technology, Cairo, Egypt, 5–6 December 2005. [[CrossRef](#)]
40. Salem, M.S.; Salem, M.S.; Zekry, A.A.; Ragai, H.F. Determining the Required Pulses for Controlling the Operation of Electrostatic MEMS Converters. In Proceedings of the 2006 International Conference on MEMS, NANO, and Smart Systems, Cairo, Egypt, 27–29 December 2006. [[CrossRef](#)]
41. Salem, M.S.; Tasciuc, D.B.; Zekry, A.A.; Ragai, H.F. Fabrication and Test of Electrostatic MEMS Converter Found in Energy Scavenging Systems. *Adv. Mater. Res.* **2012**, *403*, 4557–4563. [[CrossRef](#)]
42. Tousif, S.R. MEMS Wideband Energy Harvesting Using Nonlinear Springs and Mechanical Stoppers. Ph.D. Thesis, The University of Texas, Arlington, TX, USA, 2019.
43. Oxaal, J.; Hella, M.; Borca-Tasciuc, D.A. Electrostatic MEMS vibration energy harvester for HVAC applications with impact-based frequency up-conversion. *J. Micromech. Microeng.* **2016**, *26*, 124012. [[CrossRef](#)]
44. Roundy, S.J. Energy Scavenging for Wireless Sensor Nodes with a Focus on Vibration to Electricity Conversion. Ph.D. Thesis, University of California, Berkeley, CA, USA, 2003.

45. Mur Miranda, J.O. Electrostatic Vibration-to-Electric Energy Conversion. Ph.D. Thesis, Massachusetts Institute of Technology, Cambridge, MA, USA, 2004.
46. Isaiah, T.G.; Dabbashi, S.; Bosak, D.; Sampath, S.; Di Lorenzo, G.; Pilidis, P. Life analysis of industrial gas turbines used as a back-up to renewable energy sources. *Procedia CIRP* **2015**, *38*, 239–244. [[CrossRef](#)]
47. 0.35u CMOS Technology. Available online: https://edisciplinas.usp.br/pluginfile.php/5354646/mod_resource/content/1/ENG-182_rev2.pdf (accessed on 1 April 2022).
48. Abd Alameer, M.F.; Khalaf, T.H. Computational analysis for electrical breakdown in air due to streamer discharge in rod-to-plane arrangement. *IOP Conf. Ser. Mater. Sci. Eng.* **2020**, *757*, 012018. [[CrossRef](#)]
49. Ezhilvalavan, S.; Tseng, T.Y. Preparation and properties of tantalum pentoxide (Ta₂O₅) thin films for ultra large scale integrated circuits (ULSIs) application—A review. *Mater. Sci. Mater. Electron.* **1999**, *10*, 9–31. [[CrossRef](#)]
50. Paskaleva, A.; Atanassova, E.; Dimitrova, T. Leakage currents and conduction mechanisms of Ta₂O₅ layers on Si obtained by RF sputtering. *Vacuum* **2000**, *58*, 470–477. [[CrossRef](#)]
51. Aygun, G.; Turan, R. Electrical and dielectrical properties of tantalum oxide films grown by Nd: YAG laser assisted oxidation. *Thin Solid Films* **2008**, *517*, 994–999. [[CrossRef](#)]
52. Riaz, A.; Sarker, M.R.; Saad, M.H.M.; Mohamed, R. Review on comparison of different energy storage technologies used in micro-energy harvesting, WSNs, low-cost microelectronic devices: Challenges and recommendations. *Sensors* **2021**, *21*, 5041. [[CrossRef](#)]